

A general method to fine-tune fluorophores for live-cell and *in vivo* imaging

Jonathan B Grimm, Anand K Muthusamy, Yajie Liang, Timothy A Brown, William C Lemon[✉], Ronak Patel, Rongwen Lu, John J Macklin, Philipp J Keller[✉], Na Ji & Luke D Lavis[✉]

Pushing the frontier of fluorescence microscopy requires the design of enhanced fluorophores with finely tuned properties. We recently discovered that incorporation of four-membered azetidine rings into classic fluorophore structures elicits substantial increases in brightness and photostability, resulting in the Janelia Fluor (JF) series of dyes. We refined and extended this strategy, finding that incorporation of 3-substituted azetidine groups allows rational tuning of the spectral and chemical properties of rhodamine dyes with unprecedented precision. This strategy allowed us to establish principles for fine-tuning the properties of fluorophores and to develop a palette of new fluorescent and fluorogenic labels with excitation ranging from blue to the far-red. Our results demonstrate the versatility of these new dyes in cells, tissues and animals.

Small molecule fluorophores are essential tools for biochemical and biological imaging^{1,2}. The development of new labeling strategies³ and innovative microscopy techniques⁴ is driving the need for new fluorophores with specific properties. A particularly useful class of dyes is the rhodamines, first reported in 1887 (ref. 5) and now used extensively because of the superb brightness and excellent photostability of this fluorophore scaffold^{1,2,6}. The photophysical and chemical properties of rhodamines can be modified through chemical substitution^{6–14}, allowing the creation of fluorescent and fluorogenic labels, indicators and stains in different colors^{7,11–20}.

Despite a century of work on this dye class, the design and synthesis of new rhodamines remains severely limited by chemistry. The classic method of rhodamine synthesis—acid-catalyzed condensation^{2,5,6}—is incompatible with all but the simplest functional groups. To remedy this long-standing problem, our laboratory developed a method to synthesize rhodamine dyes using a Pd-catalyzed cross-coupling strategy starting from simple fluorescein derivatives²¹. This approach facilitated the discovery of a previously unknown class of dyes containing four-membered azetidine rings, which exhibit substantial increases in the quantum yield relative to classic rhodamines containing *N,N*-dimethylamino

groups¹³. The flagship member of this new dye class is Janelia Fluor 549 (JF₅₄₉, **1**; Fig. 1a). The enhanced brightness and photostability of this rhodamine dye has made it an exceptionally useful label for single-molecule experiments in living cells^{13,22–25}; the recent development of a photoactivatable derivative has further extended its utility in advanced imaging experiments²⁶.

An important feature of rhodamine dyes is the ability to tune the spectral and chemical properties using chemistry¹³. JF₅₄₉ (**1**; Fig. 1a and Table 1) absorbs green light ($\lambda_{\text{abs}}/\lambda_{\text{em}} = 549 \text{ nm}/571 \text{ nm}$, absolute fluorescence quantum yield value (Φ) = 0.88), making it an excellent match for light sources centered near 550 nm. Replacing the xanthene oxygen in JF₅₄₉ (**1**) with a quaternary carbon yields carborhodamine Janelia Fluor 608 (JF₆₀₈, **2**), with an expected⁸ 59-nm shift in spectral properties ($\lambda_{\text{abs}}/\lambda_{\text{em}} = 608 \text{ nm}/631 \text{ nm}$, $\Phi = 0.67$). A larger red-shift can be achieved using the established Si-rhodamine strategy^{10,12} to yield Janelia Fluor 646 (JF₆₄₆, **3**, $\lambda_{\text{abs}}/\lambda_{\text{em}} = 646 \text{ nm}/664 \text{ nm}$, $\Phi = 0.54$). Finally, a shift to shorter wavelengths can be imposed by replacing one azetidine group in JF₅₄₉ (**1**) with an oxygen atom to yield rhodol²⁷ Janelia Fluor 519 (JF₅₁₉, **4**, $\lambda_{\text{abs}}/\lambda_{\text{em}} = 519 \text{ nm}/546 \text{ nm}$, $\Phi = 0.85$).

In addition to large shifts in λ_{abs} and λ_{em} , these modifications modulate the equilibrium between the colorless, nonfluorescent, ‘closed’ lactone (L) form and the colored, fluorescent, ‘open’ zwitterionic (Z) form. Rhodamine JF₅₄₉ (**1**, $\epsilon = 1.01 \times 10^5 \text{ M}^{-1} \text{ cm}^{-1}$), carborhodamine JF₆₀₈ (**2**, $\epsilon = 9.9 \times 10^4 \text{ M}^{-1} \text{ cm}^{-1}$) and rhodol JF₅₁₉ (**4**, $\epsilon = 5.9 \times 10^4 \text{ M}^{-1} \text{ cm}^{-1}$) primarily adopt the open, zwitterionic form in water, as evidenced by their large extinction coefficients (ϵ ; Table 1). In contrast, JF₆₄₆ (**3**) predominantly adopts the colorless, nonfluorescent and lipophilic lactone form in aqueous solution ($\epsilon = 5.0 \times 10^3 \text{ M}^{-1} \text{ cm}^{-1}$). The shifted L-Z equilibrium of JF₆₄₆ and other Si-rhodamines renders these dyes highly cell permeable as well as chromogenic and fluorogenic, where the change in chemical environment after binding of dye ligands to a variety of biomolecular targets can shift the equilibrium to the fluorescent zwitterionic form^{12–14,18}.

The strategies described above allow only ‘coarse’ tuning of spectral and chemical attributes: spectral shifts >30 nm and substantial changes in L-Z equilibrium and absorptivity. We developed

Janelia Research Campus, Howard Hughes Medical Institute, Ashburn, Virginia, USA. Correspondence should be addressed to L.D.L. (lavisl@janelia.hhmi.org).

RECEIVED 14 APRIL; ACCEPTED 25 JULY; PUBLISHED ONLINE 4 SEPTEMBER 2017; DOI:10.1038/NMETH.4403

a general method to finely tune the spectral and chemical properties of rhodamine dyes with unprecedented precision. The use of 3-substituted azetidines on the Janelia Fluor 549 (**1**) scaffold allows modulation of λ_{abs} , λ_{em} and the L-Z equilibrium without affecting fluorescence quantum yield. The shifts in chemical and spectral properties can be explained using physical organic chemistry principles and computational chemistry. The structure-activity relationships that we determined for rhodamine dyes were generalizable to related structures, allowing the rational design of four new fluorophores aligned with standard laser excitation sources across the visible spectrum: rhodol JF₅₀₃, rhodamine JF₅₂₅, carborhodamine JF₅₈₅ and Si-rhodamine JF₆₃₅. These dyes exhibited improved properties for cellular imaging and could be extended to applications in tissue or *in vivo*.

RESULTS

Fine-tuning rhodamines: Janelia Fluor 525

We reasoned that we could finely tune the physicochemical properties of JF₅₄₉ (**1**) by exploring different substitution patterns on the azetidine ring. Indeed, the azetidinyl-rhodamine system provides an ideal test case for N-substituent effects because of the high-yielding Pd-catalyzed cross-coupling synthesis²¹; the commercial availability of assorted 3-substituted azetidines; the short, three-bond separation between the substituent and the rhodamine aniline nitrogen; and the symmetry of the system. We hypothesized that electron-withdrawing groups would decrease the λ_{abs} of the fluorophore and shift the L-Z equilibrium toward the closed, colorless lactone form based on initial computational chemistry experiments (Fig. 1b and Online Methods) and reports of fluoroalkane-substituted rhodamine dyes^{19,28}.

To test these predictions, we synthesized compounds 5–12 (Fig. 1a and Table 1) using our Pd-catalyzed cross-coupling approach^{13,21}. We then evaluated the photophysical properties of compounds 5–12 in aqueous solution, comparing them with JF₅₄₉ (**1**; Table 1). All of the substituted azetidinyl dyes showed high ϵ values above $1 \times 10^5 \text{ M}^{-1} \text{ cm}^{-1}$ except for the 3,3-difluoroazetidine compound **12**, which exhibited a slightly lower absorptivity ($\epsilon = 9.4 \times 10^4 \text{ M}^{-1} \text{ cm}^{-1}$). Similarly, the quantum yield values of the azetidine dyes 5–12 were all >0.80, with the exception of the *N,N*-dimethyl-azetidin-3-amine compound **8**, which showed $\Phi = 0.57$ at pH 7.4. The quantum yield value for **8** was rescued at pH 5.0 ($\Phi = 0.89$; Table 1), which is suggestive of photoinduced electron transfer (PeT) quenching by the unprotonated dimethylamino groups²⁹.

Although the ϵ and Φ of the different azetidinyl-rhodamine dyes was largely immune to substitution at the 3-position, the λ_{abs} and λ_{em} values were strongly affected by the nature of the substituent (Table 1 and Supplementary Fig. 1). Groups with greater electron-withdrawing character elicited larger hypsochromic shifts in λ_{abs} . This effect was additive. For example, the 3-fluoroazetidinyl compound **10** showed a 13-nm blue shift ($\lambda_{\text{abs}} = 536 \text{ nm}$) relative to the parent dye (**1**), and the 3,3-difluoroazetidinyl-rhodamine (**12**) showed a further hypsochromic shift of 11 nm ($\lambda_{\text{abs}} = 525 \text{ nm}$). We plotted λ_{abs} against the available Hammett inductive substituent constants (σ_1)³⁰ for the azetidine substituents in dyes **1**, **5** and **8–12** and observed an excellent correlation (Fig. 1c), suggesting that the inductive effect of the substituents was primarily responsible for the decrease in absorption and emission maxima. The experimental λ_{abs} values also showed excellent agreement with calculated λ_{abs} values (Fig. 1b).

We then analyzed how the azetidine substitutions can tune the L-Z equilibrium (Fig. 1d), first examining the absorbance of fluorophores **1**, **5** and **9–12** as a function of dielectric constant using dioxane-water titrations^{11,16} (Fig. 1e); compounds **6–8** were not examined as a result of the ionizable substituents on the azetidine ring. On the basis of these data, we determined the equilibrium constant ($K_{\text{L-Z}}$)³¹ in 1:1 dioxane:water, which gave the largest distribution of absorbance measurements (Fig. 1f), and therefore $K_{\text{L-Z}}$ values (Fig. 1d and Table 1). We determined these equilibrium values from the maximal extinction coefficients (ϵ_{max}) measured in acidic alcohol solutions (Table 1 and Online Methods). JF₅₄₉ (**1**) and the 3,3-dimethylazetidinyl-rhodamine (**5**) showed $K_{\text{L-Z}}$ values >3, indicating that these dyes exist primarily in the open form. In contrast, the equilibrium constant of the 3,3-difluoroazetidinyl-rhodamine (**12**) was substantially smaller ($K_{\text{L-Z}} = 0.068$), suggesting that the electron-withdrawing fluorine substituents can shift the equilibrium toward the closed lactone form. The remainder of the dyes exhibited $K_{\text{L-Z}}$ values that were intermediate and correlated with σ_1 (Fig. 1g). Collectively, these results yield rational and general rules for tuning both λ_{abs} and the L-Z equilibrium using different 3-substituted azetidines without compromising fluorophore brightness.

Rhodamine **12** exhibited λ_{abs} at 525 nm and a high quantum yield ($\Phi = 0.91$), making it a useful label for imaging with blue-green excitation (514–532 nm). On the basis of the λ_{abs} , we named this fluorophore Janelia Fluor 525 (JF₅₂₅) and prepared the JF₅₂₅-HaloTag³² ligand (**13**; Fig. 1h), which showed excellent labeling in live cells expressing histone H2B-HaloTag fusions (Fig. 1i). We posited that the JF₅₂₅-HaloTag ligand (**13**) would show improved cell permeability relative to the parent JF₅₄₉-HaloTag ligand (**14**; Fig. 1h) based on its higher propensity to adopt the lactone form (Fig. 1d–f and Table 1). We compared the labeling efficiency of **13** or JF₅₄₉-HaloTag ligand **14** in live cells expressing HaloTag-histone H2B fusions (Online Methods). Compound **13** labeled intracellular proteins faster than JF₅₄₉ ligand **14** (Fig. 1j). These results support the hypothesis that shifting the L-Z equilibrium toward the lactone form can improve cell permeability. We also synthesized the JF₅₂₅-SNAP-tag ligand **15**, which was useful for intracellular labeling (Supplementary Fig. 2a,b), validating JF₅₂₅ as the first cell-permeable self-labeling tag ligand with an excitation maximum near 532 nm. None of the reported HaloTag or SNAP-tag ligands showed acute cellular toxicity at standard labeling concentrations and incubation times (Supplementary Fig. 2c).

Fine-tuning rhodols: Janelia Fluor 503

Since fluorine is the most electronegative atom, the difluoroazetidine-containing JF₅₂₅ (**12**) represents the tuning limit of the azetidinyl-rhodamines toward the blue region of the spectrum. To access shorter wavelength dyes, we turned to the rhodol Janelia Fluor 519 (**4**; Figs. 1a and 2a). On the basis of the tuning rules that we determined for the rhodamine dyes (Fig. 1a), we surmised that replacement of the single azetidine substituent with a 3,3-difluoroazetidine could elicit a desirable ~15-nm blue-shift to yield a dye with maximal absorption closer to 488 nm. To test this hypothesis, we synthesized the 3,3-difluoroazetidinyl-rhodol **16**, which showed the expected blue-shifted spectra with $\lambda_{\text{abs}}/\lambda_{\text{em}} = 503 \text{ nm}/529 \text{ nm}$, $\epsilon = 8.3 \times 10^4 \text{ M}^{-1} \text{ cm}^{-1}$ and $\Phi = 0.87$ (Fig. 2a, Table 1 and Supplementary Fig. 1); we named this compound Janelia Fluor 503 (JF₅₀₃).

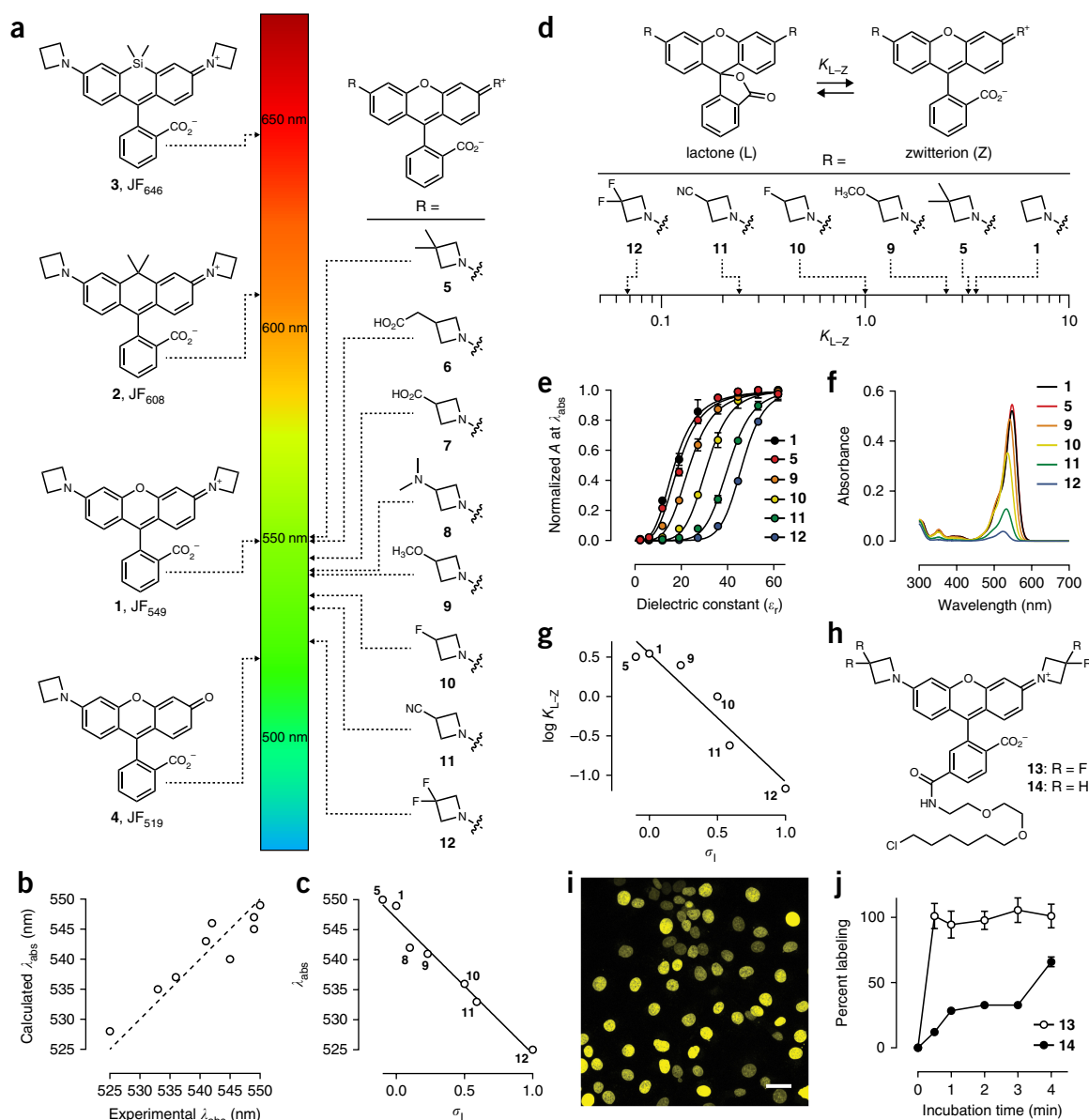


Figure 1 | Fine-tuning rhodamine dyes. (a) Comparing coarse-tuning of λ_{abs} for dyes 1–4 and fine-tuning observed for azetidinyll-rhodamines 5–12. (b) Correlation between calculated (DFT) and experimental λ_{abs} values for dyes 1, 5–12; dashed line shows ideal fit. (c) Correlation of experimental λ_{abs} versus inductive Hammett constants (σ_I) for dyes 1, 5 and 8–12. For the geminal disubstituted compounds 5 and 12, the σ_I of the substituent was doubled. Solid line shows linear regression ($R^2 = 0.97$). (d) Fine-tuning of the L-Z equilibrium constant (K_{L-Z}) for dyes 1, 5 and 9–12. (e) Normalized absorption versus dielectric constant (ϵ_r) for dyes 1, 5 and 9–12; error bars show \pm s.e.m.; $n = 4$. (f) Absolute absorbance of 1, 5 and 9–12 (5 μ M) in 1:1 dioxane:H₂O. (g) Correlation of $\log K_{L-Z}$ versus inductive Hammett constants (σ_I) for dyes 1, 5 and 9–12. For the geminal disubstituted compounds 5 and 12, the σ_I of the substituent was doubled. Solid line shows linear regression ($R^2 = 0.91$). (h) Chemical structure of JF₅₂₅-HaloTag ligand 13 and JF₅₄₉-HaloTag ligand 14. (i) Image of live, washed COS7 cells expressing histone H2B-HaloTag fusions and labeled with ligand 13. Scale bar represents 35 μ m. (j) Plot of percent labeling of histone H2B-HaloTag fusions in live cells versus incubation time for ligands 13 (100 nM) and 14 (100 nM); error bars show \pm s.e.m.; $n = 113$ –248 (Online Methods).

We then synthesized the JF₅₀₃-HaloTag ligand (17; Fig. 2b), which was an excellent label for histone H2B-HaloTag fusions in live cells (Fig. 2c). We compared this label to two other 488-nm-excited HaloTag ligands based on the classic rhodamine 110 ($\lambda_{abs}/\lambda_{em} = 497$ nm/520 nm, 18) and the recently described *N,N'*-bis(2,2,2-trifluoroethyl)rhodamine ($\lambda_{abs}/\lambda_{em} = 501$ nm/525 nm, 19; Supplementary Fig. 2d)¹⁹. The cell-loading time course for these structurally distinct and relatively polar dyes was similar (Supplementary Fig. 2e), but the JF₅₀₃ ligand showed higher

photostability than the other two dyes in live cells (Fig. 2d), consistent with previous reports comparing the photostability of rhodols to rhodamines²⁷. JF₅₀₃ could be extended to the SNAP-tag labeling system with JF₅₀₃-SNAP-tag ligand (20; Supplementary Fig. 2f,g).

Fine-tuning carbhorhodamines: Janelia Fluor 585

Previously, we extended our Pd-catalyzed cross-coupling approach to carbhorhodamines¹¹, resulting in the synthesis of JF₆₀₈ (2; Figs. 1a and 2e, and Table 1)¹³. We also discovered that carbhorhodamines

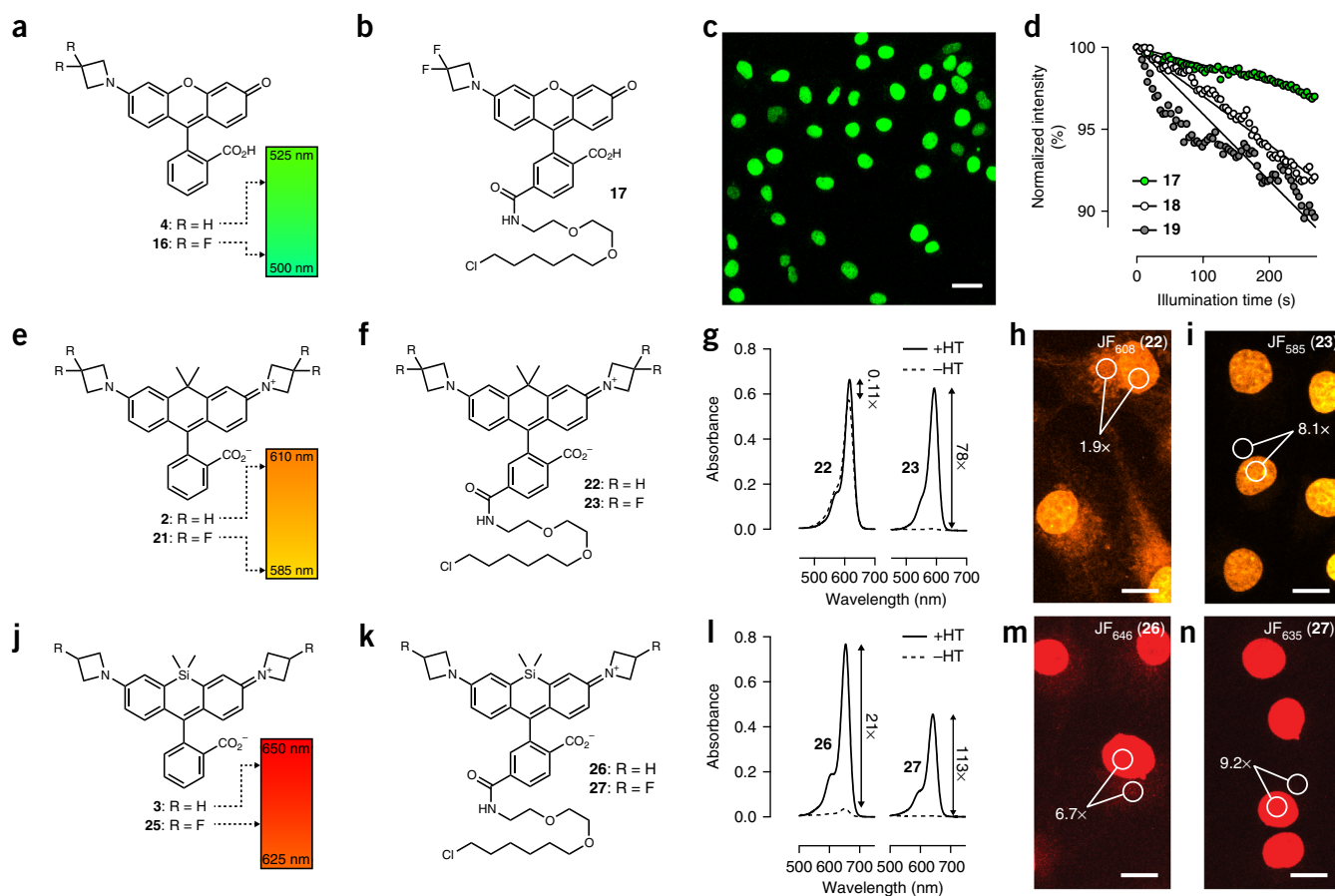


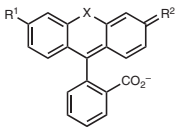
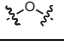
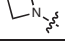
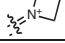
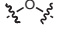

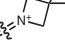
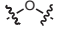


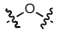

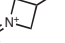
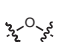
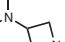
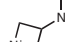
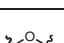
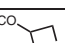
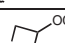
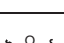


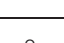
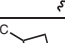
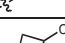
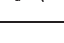
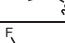
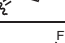
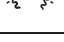
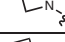
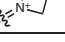
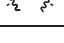

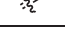
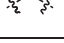
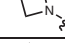
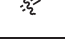
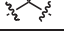
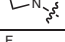
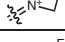
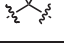

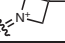
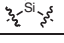
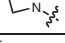
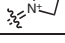
Figure 2 | Rational fine-tuning of other dyes. (a) Tuning of JF₅₁₉ (**4**) to yield JF₅₀₃ (**16**). (b) Structure of JF₅₀₃-HaloTag ligand **17**. (c) Image of live, washed COS7 cells expressing histone H2B-HaloTag fusions and labeled with ligand **17**. Scale bar represents 35 μm . (d) Comparison of the photostability of cells labeled with **17** and cells labeled with 488-nm-excited dyes **18** and **19** (Supplementary Fig. 2d); the initial photobleaching measurements are fitted to a linear regression. (e) Tuning of JF₆₀₈ (**2**) to yield JF₅₈₅ (**21**). (f) Structure of HaloTag ligands derived from JF₆₀₈ (**22**) and JF₅₈₅ (**23**). (g) Absorbance of HaloTag ligands **22** and **23** in the presence (+HT) or absence (–HT) of excess HaloTag protein; $n = 2$. (h, i) Representative images of COS7 cells expressing HaloTag-histone H2B fusion, labeled with 250 nM of HaloTag ligands **22** and **23** for 1 h and imaged directly without washing. The image for each dye pair was taken with identical microscope settings, $\lambda_{\text{ex}} = 594 \text{ nm}$. Numbers indicate mean signal (nuclear) to background (cytosol) ratio (S/B) in three fields of view. (h) JF₆₀₈ ligand **22** (S/B from $n = 224$ areas). (i) JF₅₈₅ ligand **23** (S/B from $n = 235$ areas). (j) Tuning of JF₆₄₆ (**3**) to yield JF₆₃₅ (**25**). (k) Structure of HaloTag ligands derived from JF₆₄₆ (**26**) and JF₆₃₅ (**27**). (l) Absorbance of HaloTag ligands **26** and **27** in the presence (+HT) or absence (–HT) of excess HaloTag protein ($n = 2$). (m, n) Representative images of COS7 cells expressing HaloTag-histone H2B fusion, labeled with 250 nM of HaloTag ligands **26** and **27** for 1 h and imaged directly without washing. The image for each dye pair was taken with identical microscope settings, $\lambda_{\text{ex}} = 647 \text{ nm}$. Numbers indicate mean signal (nuclear) to background (cytosol) ratio in three fields of view. (m) JF₆₄₆ ligand **26** (S/B from $n = 175$ areas). (n) JF₆₃₅ ligand **27** (S/B from $n = 278$ areas). Scale bars in **h**, **i**, **m** and **n** represent 15 μm .

generally exhibit a higher propensity to adopt the colorless lactone form compared with rhodamines ($K_{\text{L-Z}}$ for **2** = 0.091). Nevertheless, this shift in the L-Z equilibrium is not sufficient to achieve fluorogenic ligands and its relatively long λ_{abs} value makes JF₆₀₈ suboptimal for multicolor cellular imaging experiments using orange (589 nm) and red (640 nm) excitation. Based on the rhodamine tuning (Fig. 1a), we expected that incorporation of a 3,3-difluoroazetidine would elicit a blue-shift of approximately 24 nm, bringing the λ_{abs} closer to the desired excitation wavelengths. We were also curious whether this modification would create a fluorogenic label given that, in the rhodamine series, the 3,3-difluoroazetidine motif decreased the $K_{\text{L-Z}}$ by nearly two log units (Fig. 1d). Given the linear relationship between $\log K_{\text{L-Z}}$ and σ_{I} (Fig. 1g) we reasoned that this substitution should tune the equilibrium of JF₆₀₈ (**2**, $K_{\text{L-Z}} = 0.091$) closer to the fluorogenic JF₆₄₆ (**3**, $K_{\text{L-Z}} = 0.0012$; Table 1). We note previous efforts to shift the L-Z equilibrium of carborhodamines using direct fluorination

produced a HaloTag ligand with modest, nine-fold fluorogenicity, but also severely decreased quantum yield¹⁹. On the basis of the general trend to higher Φ values following incorporation of electron-withdrawing substituents in both rhodamines and rhodols (Table 1), we expected that substitution with fluorine atoms on the 3-position of azetidine would also increase quantum yield of carborhodamines.

To test these predictions, we synthesized the 3,3-difluoroazetidyl-carborhodamine (**21**), which showed the expected blue-shift in spectra ($\lambda_{\text{abs}}/\lambda_{\text{em}} = 585 \text{ nm}/609 \text{ nm}$) and increase in quantum yield ($\Phi = 0.78$; Fig. 2e, Table 1 and Supplementary Fig. 1). Based on these properties the dye was named ‘Janelia Fluor 585’ (JF₅₈₅). As predicted, JF₅₈₅ (**21**) also exhibited low visible absorption in water ($\epsilon = 1.5 \times 10^3 \text{ M}^{-1} \text{ cm}^{-1}$) and a $K_{\text{L-Z}}$ near zero (Table 1). We then evaluated these carborhodamines as biomolecule labels, preparing JF₆₀₈-HaloTag ligand (**22**) and JF₅₈₅-HaloTag ligand (**23**; Fig. 2f)^{11,13,21}. We first determined the absorbance of these

Table 1 | Properties of azetidine-containing fluorophores **1–12**, **16**, **21** and **25**

									
Dye	X	R ¹	R ²	λ_{abs} (nm)	ϵ (M ⁻¹ cm ⁻¹)	ϵ_{max} (M ⁻¹ cm ⁻¹) ^a	λ_{em} (nm)	Φ	$K_{\text{L-Z}}$ ^b
1 (JF ₅₄₉)				549	101,000	134,000	571	0.88	3.5
5				550	110,000	143,000	572	0.83	3.2
6				549	111,000	138,000	572	0.87	–
7				545	108,000	130,000	568	0.87	–
8				542	111,000	127,000	565	0.57 ^c	–
9				541	109,000	137,000	564	0.88	2.5
10				536	113,000	141,000	560	0.87	1.0
11				533	108,000	133,000	557	0.89	0.24
12 (JF ₅₂₅)				525	94,000	122,000	549	0.91	0.068
4 (JF ₅₁₉)				519	59,000	69,000	546	0.85	–
16 (JF ₅₀₃)				503	83,000	95,000	529	0.87	–
2 (JF ₆₀₈)				608	99,000	121,000	631	0.67	0.091
21 (JF ₅₈₅)				585	1,500	156,000	609	0.78	<0.0001
3 (JF ₆₄₆)				646	5,000	152,000	664	0.54	0.0012
25 (JF ₆₃₅)				635	~400	167,000	652	0.56	<0.0001

^aMaximal extinction coefficient measured in ethanol or TFE with 0.1% TFA (rhodamines) or 0.01% Et₃N (rhodols). ^bEquilibrium constant measured in 1:1 (vol/vol) dioxane:water. ^c Φ = 0.89 in pH 5.0 buffer.

ligands in the absence and presence of excess HaloTag protein. JF₆₀₈-HaloTag ligand (**22**) showed only an 11% increase in absorption following reaction with the HaloTag protein, but JF₅₈₅ ligand **23** showed a substantially higher absorbance increase of 80-fold (Fig. 2g). We then evaluated these dyes in ‘no wash’ cellular imaging experiments. Incubation of JF₆₀₈-HaloTag ligand (**22**, 250 nM) with cells expressing histone H2B-HaloTag showed excellent nuclear labeling, but high background, as a result of the free ligand staining internal membrane structures (Fig. 2h). In contrast, cells that were incubated with 250 nM of JF₅₈₅-HaloTag ligand **23** and imaged directly showed bright nuclei with low fluorescence background (Fig. 2i). The JF₅₈₅-SNAP-tag ligand (**24**) also functioned as a cellular label (Supplementary Fig. 2h,i), and the orange JF₅₈₅-HaloTag ligand (**23**) could be used in three-color experiments with the green

JF₅₀₃-SNAP-tag ligand (**20**) and our previously described red JF₆₄₆-Hoechst stain³³ (Supplementary Fig. 2j).

Fine-tuning Si-rhodamines: Janelia Fluor 635

Having success in applying these tuning rules to rhodol and carbodamine dyes, we then turned to the Si-rhodamine JF₆₄₆ (**3**; Figs. 1a and 2j)¹³. We anticipated that addition of a single fluorine atom on each azetidine ring would elicit a ~13-nm hypsochromic shift and further decrease $K_{\text{L-Z}}$, yielding a dye with a λ_{abs} near 633 nm and higher degree of fluorogenicity. True to this prediction, the synthesis of the desired fluorinated derivative **25** (Fig. 2j) afforded a dye that showed $\lambda_{\text{abs}}/\lambda_{\text{em}}$ = 635 nm/652 nm and a slightly higher Φ = 0.56 relative to JF₆₄₆ (**3**). Compound **25** also exhibited an extremely low absorbance in water with

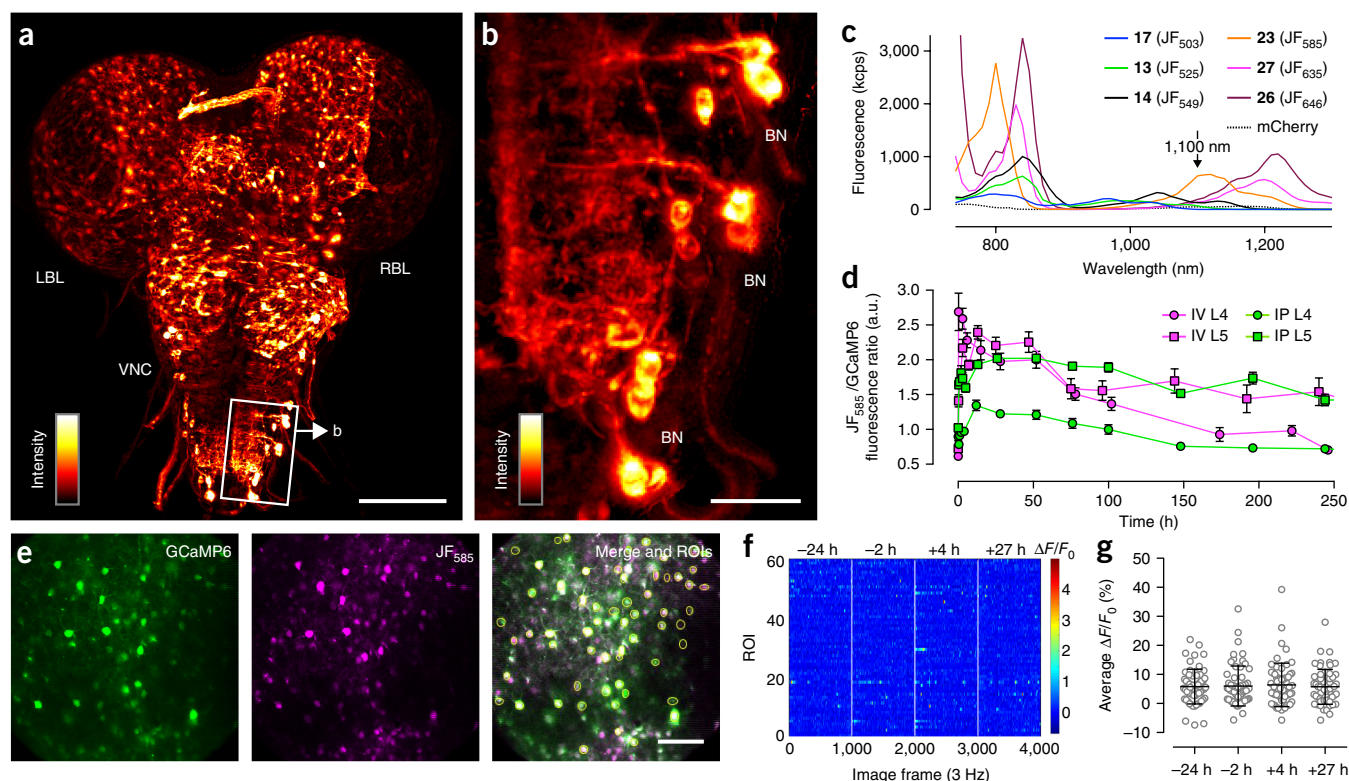


Figure 3 | Labeling in tissue and *in vivo*. (a) SiMView light-sheet microscopy image (3D projection) of the CNS of a third instar *Drosophila* larva expressing myristoylated HaloTag protein in 'Basin' neurons (BNs) and stained with JF₆₃₅-HaloTag ligand (27); LBL, left brain lobe; VNC, ventral nerve cord; RBL, right brain lobe. Scale bar represents 100 μ m. (b) Magnification of boxed area in a showing individual BN cell bodies. Scale bar represents 20 μ m. (c) Two-photon fluorescence excitation spectra of HaloTag conjugates (1 μ M) from HaloTag ligands 13, 14, 17, 23, 26 and 27 in 10 mM HEPES buffer (pH 7.3). The two-photon excitation spectra for mCherry is shown for reference. (d) Ratio of JF₅₈₅ fluorescence to GCaMP6s epifluorescence at different time points after a single IV or IP injection of JF₅₈₅-HaloTag ligand (23, 100 nmol) into mice expressing HaloTag protein in either layer 4 (L4) or layer 5 (L5) cortical neurons; $n = 3$ fields of view; error bars show \pm s.e.m. (e) Two-photon microscopy images of neurons in layer 5 of the visual cortex coexpressing GCaMP6s (green) and JF₅₈₅-labeled HaloTag (magenta) after IV injection of ligand 23 ($t = 5$ h). Scale bar represents 100 μ m. Yellow circles in the merged image indicate individual neurons as regions of interest (ROIs). (f) Raster plot of spontaneous neuronal activity in different ROIs ($n = 61$) before and after labeling with JF₅₈₅-HaloTag ligand (23). (g) Plot of average spontaneous neural activity in each ROI before and after labeling with JF₅₈₅-HaloTag ligand (23); central line shows mean; error bars show \pm s.d.; no significant difference was observed between time points (one-way ANOVA, $P = 0.95$).

an extinction coefficient value of approximately $400 \text{ M}^{-1} \text{ cm}^{-1}$, which gave a K_{L-Z} near zero (Table 1 and Supplementary Fig. 1). We call this dye Janelia Fluor 635 (JF₆₃₅).

Analogous to the experiments with JF₆₀₈ and JF₅₈₅, we synthesized the JF₆₃₅-HaloTag ligand (27) and compared it with the JF₆₄₆ ligand 26 (Fig. 2k). As reported previously¹³, ligand 26 showed a 21-fold increase in absorbance following binding to the HaloTag protein (Fig. 2l). The shifted L-Z equilibrium of JF₆₃₅ caused HaloTag ligand 27 to show exceptionally low background and a 113-fold increase in absorbance following conjugation (Fig. 2l). Both of these absorbance increases were substantially larger than the previously published SiTMR ligand 28 (Supplementary Fig. 2k), which showed a 6.7-fold increase in absorption following reaction with the HaloTag protein^{12,13}. These *in vitro* results were mirrored in no-wash cellular imaging experiments, in which we incubated cells expressing histone H2B-HaloTag fusions with 250 nM ligands 26–28. JF₆₄₆ ligand 26 (Fig. 2m) and JF₆₃₅ ligand 27 (Fig. 2n) exhibited substantially lower nonspecific extracellular fluorescence than the SiTMR compound 28 (Supplementary Fig. 2l), with JF₆₃₅ showing the highest contrast. The SNAP-tag ligand of JF₆₃₅ (29) effectively labeled SNAP-tag fusions in cells

(Supplementary Fig. 2m,n) and the JF₆₃₅-HaloTag ligand (27) could be used in a two-color experiment with JF₅₂₅-SNAP-tag ligand (15; Supplementary Fig. 2o).

Applications in tissue and *in vivo*

The HaloTag ligands of tuned fluorophores Janelia Fluor 585 (23) and Janelia Fluor 635 (27) are small, cell permeable and exhibit high fluorogenicity following reaction with the HaloTag protein. We were curious whether these properties would make them useful for labeling in more complex biological environments such as tissue or whole animals. We first attempted labeling in living brain tissue from *Drosophila* larvae using the JF₆₃₅-HaloTag ligand (27; Fig. 2k) because of its far-red excitation (Fig. 2j and Table 1) and high on/off ratio (Fig. 2l,n). We used a *Drosophila* GAL4 line expressing myristoylated HaloTag protein in 'Basin' neurons, which project basin-shaped arboris into the ventral nerve cord (VNC) of the larval fly³⁴. Explants from *Drosophila* third instar larvae were dissected, incubated briefly with 27 (1 μ M, 10 min) and imaged using the SiMView light-sheet microscope³⁵. As shown in the projection of the SiMView three-dimensional reconstruction, the JF₆₃₅ label exhibited consistent labeling throughout

the living tissue and low nonspecific background staining (Fig. 3a,b and Supplementary Fig. 3a–c), demonstrating its utility beyond simple cell culture.

We next evaluated the JF dyes in the brains of living mice. The JF₅₈₅-HaloTag ligand **23** was chosen on the basis of its high fluorogenicity (Fig. 2g,i) and superior two-photon fluorescence at 1,100-nm excitation (Fig. 3c), which is sufficiently separated from GFP-based indicators such as GCaMP6 (2-photon λ_{ex} = 940 nm)³⁶ to allow multicolor imaging. Cytosolic HaloTag protein was coexpressed in layer 4 or layer 5 visual cortex (V1) neurons with GCaMP6s via viral transduction and the mice were fitted with a chronic cranial window (Online Methods). Injection of 100 nmol of HaloTag ligand **23** into the tail vein (intravenous, IV) revealed that the JF₅₈₅ ligand was blood-brain-barrier-permeable and gave measureable labeling in the brain within 5 min, peaking around 6 h and lasting for nearly 2 weeks as measured by epifluorescence (Fig. 3d and Supplementary Fig. 3d). Subsequent intraperitoneal (IP) injection into the same set of mice also showed effective delivery to the brain, although with different pharmacokinetics in the early time points (<7 d; Fig. 3d). Under two-photon imaging, we observed that the GCaMP6s and JF₅₈₅ signals colocalized (Fig. 3e, Supplementary Fig. 3e and Supplementary Video 1), and the labeling showed no significant effect on spontaneous neuronal activity (Fig. 3f,g), establishing the utility of this fluorophore and labeling strategy *in vivo*.

DISCUSSION

Despite the broad utility of rhodamines, methods to modulate the physicochemical properties of this dye class are relatively coarse and empirical. We developed a method that allows rational fine-tuning of fluorophore properties for specific biological applications. We first determined the tuning rules in the rhodamine system by synthesizing a panel of rhodamine variants using the bright and photostable JF₅₄₉ scaffold (Fig. 1a). This resulted in the development of JF₅₂₅ (**12**) and its derivatives **13** and **15**, which constitute the first ligands for self-labeling tags with absorption maxima near 532 nm. The tuning rules that we discovered are generalizable to other fluorophore classes—rhodols, carborhodamines and Si-rhodamines—allowing the rational design of finely tuned fluorophores such as JF₅₀₃ (**16**; Fig. 2a), JF₅₈₅ (**21**; Fig. 2e) and JF₆₃₅ (**25**; Fig. 2j). Together with JF₅₄₉ (**1**) and JF₆₄₆ (**3**; Fig. 1a)¹³, we have now described six dyes that span the visible region of the spectrum and match common excitation wavelengths for fluorescence microscopy. These bright fluorophores can be used immediately for structured illumination and stimulated emission depletion imaging and could be converted to photoactivatable derivatives²⁶ for single-molecule localization microscopy experiments. Our general rules should allow fine-tuning of a variety of fluorescent reagents, including classic fluorophores¹³, emerging red-shifted rhodamine variants³⁷ and fluorogenic ligands^{12,14,18,19,33}, to further extend the range of bright fluorophores useful for fluorescence microscopy. Notably, the new HaloTag ligands derived from JF₅₈₅ and JF₆₃₅ showed a high degree of chromogenicity and fluorogenicity (Fig. 2g,i,l,n), a critical parameter in advanced imaging experiments³⁸. Of particular interest is the ability to deliver these dyes to neural tissue in explants (Fig. 3a,b) or whole animals (Fig. 3d–g), which could allow the imaging of deeper structures in the brain or the *in situ* assembly of semisynthetic indicators for monitoring cellular activity³.

Although we focused on the fluorine-substituted azetidines, the other substitutions (Fig. 1a) could be exploited to prepare fluorophores for specific applications. For example, the carboxy groups in compounds **6** and **7** could serve as attachment sites for a variety of chemical modifiers to improve solubility⁷, quench unwanted triplet states³⁹ or to allow the molecule to serve as a multivalent fluorescent cross-linker. The modest pH sensitivity and presence of the basic amine in compound **8** could allow it to function as a pH sensor or stain for lysosomes. The methoxy group on compound **9** could be elaborated to a polyethylene glycol (PEG) or another solubilizing group. Finally, the cyano group in compound **11** could be used in multimodal regimes in which both fluorescence and Raman⁴⁰ modalities are used for imaging. In all, this general method to rationally tune photophysical and chemical properties against a backdrop of high quantum yield will allow the precise design of many new fluorophores for specific, sophisticated biological imaging experiments in increasingly complex systems.

METHODS

Methods, including statements of data availability and any associated accession codes and references, are available in the [online version of the paper](#).

Note: Any Supplementary Information and Source Data files are available in the online version of the paper.

ACKNOWLEDGMENTS

We thank A. Berro and E. Schreiter (Janelia) for purified HaloTag protein, and H. Choi (Janelia) for the Sec61 β -HaloTag plasmid, contributive discussions and critical reading of the manuscript. This work was supported by the Howard Hughes Medical Institute.

AUTHOR CONTRIBUTIONS

L.D.L. and J.B.G. conceived the project. J.B.G. contributed organic synthesis and one-photon spectroscopy measurements. A.K.M. contributed organic synthesis and computational chemistry experiments. Y.L., R.L. and N.J. contributed mouse imaging experiments. T.A.B. contributed cultured cell imaging experiments. W.C.L. and P.J.K. contributed larval explant imaging experiments. R.P. and J.J.M. contributed two-photon spectroscopy measurements. L.D.L. contributed one-photon spectroscopy measurements and wrote the manuscript with input from the other authors.

COMPETING FINANCIAL INTERESTS

The authors declare competing financial interests: details are available in the [online version of the paper](#).

Reprints and permissions information is available online at <http://www.nature.com/reprints/index.html>. Publisher's note: Springer Nature remains neutral with regard to jurisdictional claims in published maps and institutional affiliations.

- Lavis, L.D. & Raines, R.T. Bright ideas for chemical biology. *ACS Chem. Biol.* **3**, 142–155 (2008).
- Lavis, L.D. & Raines, R.T. Bright building blocks for chemical biology. *ACS Chem. Biol.* **9**, 855–866 (2014).
- Xue, L., Karpenko, I.A., Hiblot, J. & Johnsson, K. Imaging and manipulating proteins in live cells through covalent labeling. *Nat. Chem. Biol.* **11**, 917–923 (2015).
- Liu, Z., Lavis, L.D. & Betzig, E. Imaging live-cell dynamics and structure at the single-molecule level. *Mol. Cell* **58**, 644–659 (2015).
- Ceresole, M. Verfahren zur Darstellung von Farbstoffen aus der Gruppe des Meta-amidophenolphthaleins. German Patent 44002 (1887).
- Beija, M., Afonso, C.A.M. & Martinho, J.M.G. Synthesis and applications of Rhodamine derivatives as fluorescent probes. *Chem. Soc. Rev.* **38**, 2410–2433 (2009).
- Panchuk-Voloshina, N. *et al.* Alexa dyes, a series of new fluorescent dyes that yield exceptionally bright, photostable conjugates. *J. Histochem. Cytochem.* **47**, 1179–1188 (1999).

8. Arden-Jacob, J., Frantzeskos, J., Kemnitzer, N.U., Zilles, A. & Drexhage, K.H. New fluorescent markers for the red region. *Spectrochim. Acta A Mol. Biomol. Spectrosc.* **57**, 2271–2283 (2001).
9. Liu, J.X. *et al.* Rational design and synthesis of a novel class of highly fluorescent rhodamine dyes that have strong absorption at long wavelengths. *Tetrahedr. Lett.* **44**, 4355–4359 (2003).
10. Koide, Y., Urano, Y., Hanaoka, K., Terai, T. & Nagano, T. Evolution of group 14 rhodamines as platforms for near-infrared fluorescence probes utilizing photoinduced electron transfer. *ACS Chem. Biol.* **6**, 600–608 (2011).
11. Grimm, J.B. *et al.* Carbofluoresceins and carborhodamines as scaffolds for high-contrast fluorogenic probes. *ACS Chem. Biol.* **8**, 1303–1310 (2013).
12. Lukinavicius, G. *et al.* A near-infrared fluorophore for live-cell super-resolution microscopy of cellular proteins. *Nat. Chem.* **5**, 132–139 (2013).
13. Grimm, J.B. *et al.* A general method to improve fluorophores for live-cell and single-molecule microscopy. *Nat. Methods* **12**, 244–250, 3, 250 (2015).
14. Lukinavicius, G. *et al.* Fluorogenic probes for multicolor imaging in living cells. *J. Am. Chem. Soc.* **138**, 9365–9368 (2016).
15. Lavis, L.D., Chao, T.-Y. & Raines, R.T. Fluorogenic label for biomolecular imaging. *ACS Chem. Biol.* **1**, 252–260 (2006).
16. Watkins, R.W., Lavis, L.D., Kung, V.M., Los, G.V. & Raines, R.T. Fluorogenic affinity label for the facile, rapid imaging of proteins in live cells. *Org. Biomol. Chem.* **7**, 3969–3975 (2009).
17. Wysocki, L.M. *et al.* Facile and general synthesis of photoactivatable xanthene dyes. *Angew. Chem. Int. Ed. Engl.* **50**, 11206–11209 (2011).
18. Lukinavicius, G. *et al.* Fluorogenic probes for live-cell imaging of the cytoskeleton. *Nat. Methods* **11**, 731–733 (2014).
19. Butkevich, A.N. *et al.* Fluorescent rhodamines and fluorogenic carbopyronines for super-resolution STED microscopy in living cells. *Angew. Chem. Int. Ed. Engl.* **55**, 3290–3294 (2016).
20. Grimm, J.B. *et al.* Synthesis of a far-red photoactivatable silicon-containing rhodamine for super-resolution microscopy. *Angew. Chem. Int. Ed. Engl.* **55**, 1723–1727 (2016).
21. Grimm, J.B. & Lavis, L.D. Synthesis of rhodamines from fluoresceins using Pd-catalyzed C-N cross-coupling. *Org. Lett.* **13**, 6354–6357 (2011).
22. Liu, Z. *et al.* 3D imaging of Sox2 enhancer clusters in embryonic stem cells. *eLife* **3**, e04236 (2014).
23. Knight, S.C. *et al.* Dynamics of CRISPR-Cas9 genome interrogation in living cells. *Science* **350**, 823–826 (2015).
24. Swinstead, E.E. *et al.* Steroid receptors reprogram FoxA1 occupancy through dynamic chromatin transitions. *Cell* **165**, 593–605 (2016).
25. Bisson-Filho, A.W. *et al.* Treadmilling by FtsZ filaments drives peptidoglycan synthesis and bacterial cell division. *Science* **355**, 739–743 (2017).
26. Grimm, J.B. *et al.* Bright photoactivatable fluorophores for single-molecule imaging. *Nat. Methods* **13**, 985–988 (2016).
27. Whitaker, J.E. *et al.* Fluorescent rhodol derivatives: versatile, photostable labels and tracers. *Anal. Biochem.* **207**, 267–279 (1992).
28. Mitronova, G.Y. *et al.* New fluorinated rhodamines for optical microscopy and nanoscopy. *Chemistry* **16**, 4477–4488 (2010).
29. Asanuma, D. *et al.* Acidic-pH-activatable fluorescence probes for visualizing exocytosis dynamics. *Angew. Chem. Int. Ed. Engl.* **53**, 6085–6089 (2014).
30. Hansch, C., Leo, A. & Taft, R.W. A survey of Hammett substituent constants and resonance and field parameters. *Chem. Rev.* **91**, 165–195 (1991).
31. Hinckley, D.A. & Seybold, P.G. A spectroscopic/thermodynamic study of the rhodamine B lactone-zwitterion equilibrium. *Spectrochim. Acta A Mol. Biomol. Spectrosc.* **44**, 1053–1059 (1988).
32. Los, G.V. *et al.* HaloTag: a novel protein labeling technology for cell imaging and protein analysis. *ACS Chem. Biol.* **3**, 373–382 (2008).
33. Legant, W.R. *et al.* High-density three-dimensional localization microscopy across large volumes. *Nat. Methods* **13**, 359–365 (2016).
34. Ohshima, T. *et al.* A multilevel multimodal circuit enhances action selection in *Drosophila*. *Nature* **520**, 633–639 (2015).
35. Lemon, W.C. *et al.* Whole-central nervous system functional imaging in larval *Drosophila*. *Nat. Commun.* **6**, 7924 (2015).
36. Chen, T.W. *et al.* Ultrasensitive fluorescent proteins for imaging neuronal activity. *Nature* **499**, 295–300 (2013).
37. Zhou, X., Lai, R., Beck, J.R., Li, H. & Stains, C.I. Nebraska Red: a phosphinate-based near-infrared fluorophore scaffold for chemical biology applications. *Chem. Commun. (Camb.)* **52**, 12290–12293 (2016).
38. Bruchez, M.P. Dark dyes-bright complexes: fluorogenic protein labeling. *Curr. Opin. Chem. Biol.* **27**, 18–23 (2015).
39. Altman, R.B. *et al.* Cyanine fluorophore derivatives with enhanced photostability. *Nat. Methods* **9**, 68–71 (2011).
40. Palonpon, A.F., Sodeoka, M. & Fujita, K. Molecular imaging of live cells by Raman microscopy. *Curr. Opin. Chem. Biol.* **17**, 708–715 (2013).

ONLINE METHODS

Chemical synthesis. Methods for chemical synthesis and full characterization of all novel compounds can be found in the **Supplementary Note**.

UV-vis and fluorescence spectroscopy. Fluorescent and fluorogenic molecules for spectroscopy were prepared as stock solutions in DMSO and diluted such that the DMSO concentration did not exceed 1% (vol/vol). Spectroscopy was performed using 1-cm path length, 3.5-ml quartz cuvettes or 1-cm path length, 1.0-ml quartz microcuvettes from Starna Cells. All measurements were taken at ambient temperature (22 ± 2 °C). Absorption spectra were recorded on a Cary Model 100 spectrometer (Agilent). Fluorescence spectra were recorded on a Cary Eclipse fluorometer (Varian). Maximum absorption wavelength (λ_{abs}), extinction coefficient (ϵ), and maximum emission wavelength (λ_{em}) were taken in 10 mM HEPES, pH 7.3 buffer unless otherwise noted; reported values for ϵ are averages ($n = 3$). Normalized spectra are shown for clarity.

Determination $K_{\text{L-Z}}$ and ϵ_{max} . To determine $K_{\text{L-Z}}$ we first performed dioxane-H₂O titrations in spectral grade dioxane (Aldrich) and milliQ H₂O (**Fig. 1e**). The solvent mixtures contained 0.01% (vol/vol) triethylamine to ensure the rhodamine dyes were in the zwitterionic form. The absorbance values at λ_{abs} were measured on 5 μM samples ($n = 4$) using a quartz 96-well microplate (Hellma) and a FlexStation3 microplate reader (Molecular Devices). Values of dielectric constant (ϵ_{r}) were as previously reported⁴¹. We then calculated $K_{\text{L-Z}}$ using the following equation³¹: $K_{\text{L-Z}} = (\epsilon_{\text{dw}}/\epsilon_{\text{max}})/(1 - \epsilon_{\text{dw}}/\epsilon_{\text{max}})$. ϵ_{dw} is the extinction coefficient of the dyes in a 1:1 (vol/vol) dioxane:water solvent mixture (**Fig. 1f**); this dioxane-water mixture was chosen to give the maximum spread of $K_{\text{L-Z}}$ values (**Fig. 1e**). ϵ_{max} is the maximal extinction coefficients measured in different solvent mixtures depending on dye type: 0.1% (vol/vol) trifluoroacetic acid (TFA) in 2,2,2-trifluoroethanol (TFE) for the rhodamines (**1**, **5–12**) and carborhodamines (**2**, **21**); 0.1% (vol/vol) TFA in ethanol for the Si-rhodamines (**3**, **25**); 0.01% (vol/vol) Et₃N in TFE for the rhodols (**4**, **16**).

Quantum yield determination. All reported absolute fluorescence quantum yield values (Φ) were measured in our laboratory under identical conditions using a Quantaaurus-QY spectrometer (model C11374, Hamamatsu). This instrument uses an integrating sphere to determine photons absorbed and emitted by a sample. Measurements were carried out using dilute samples ($A < 0.1$) and self-absorption corrections⁴² were performed using the instrument software. Reported values are averages ($n = 3$). The quantum yield for compound **8** at pH 5.0 was taken in 10 mM sodium citrate buffer containing 150 mM NaCl.

Computational chemistry. Computational experiments were performed using Gaussian 09 (ref. 43). DFT and TD-DFT methods were used to calculate the spectral properties of the azetidinyrhodamine compounds (**Fig. 1b**). Calculations were performed at the B3LYP/6-31+G(d,p)/IEFPCM and TD-B3LYP/6-31+G(d,p)/IEFPCM theory levels for the ground states and excited states respectively. Frequency calculations confirmed that an energy minimum was found in geometry optimizations. Linear response

solvation with the IEFPCM model was sufficient to study the excited state energies. Evaluations of TD-DFT theory have discussed the overestimation of excitation energies^{44,45}, and previous studies of rhodamine excited states have reported using ~ 0.4 -eV correction to account for this overestimation^{46,47}. We applied a consistent -0.4 -eV correction to the calculated excited state energies, which gave good agreement with spectroscopy experiments (**Fig. 1b**).

Measurement of increase in absorbance of HaloTag ligands **22, **23**, **26–28** following attachment with HaloTag protein.** HaloTag protein used as a 100 μM solution in 75 mM NaCl, 50 mM TRIS-HCl, pH 7.4 with 50% v/v glycerol (TBS-glycerol). Absorbance measurements were performed in 1.0-ml quartz cuvettes. HaloTag ligands **22**, **23**, **26–28** (5 μM) were dissolved in 10 mM HEPES, pH 7.3 containing 0.1 mg ml⁻¹ CHAPS. An aliquot of HaloTag protein (1.5 equiv) or an equivalent volume of TBS-glycerol blank was added and the resulting mixture was incubated until consistent absorbance signal was observed (~ 60 min). Absorbance scans are averages ($n = 2$).

Multiphoton spectroscopy. HaloTag ligands **13**, **14**, **17**, **23**, **26** and **27** (5 μM) were incubated with excess purified HaloTag protein (1.5 equiv) in 10 mM HEPES, pH 7.3 containing 0.1 mg ml⁻¹ CHAPS as above and incubated for 24 h at 4 °C. These solutions were then diluted to 1 μM in 10 mM HEPES buffer, pH 7.3 and the two-photon excitation spectra were measured as previously described^{48,49}. Briefly, measurements were taken on an inverted microscope (IX81, Olympus) equipped with a 60 \times , 1.2 NA water objective (Olympus). Dye-protein samples were excited with pulses from an 80 MHz Ti-Sapphire laser (Chameleon Ultra II, Coherent) for 710–1080 nm and with an OPO (Chameleon Compact OPO, Coherent) for 1,000–1,300 nm. Fluorescence collected by the objective was passed through a dichroic filter (675DCSXR, Omega) and a short pass filter (720SP, Semrock) and detected by a fiber-coupled Avalanche Photodiode (SPCM_AQRH-14, PerkinElmer). For reference, a two-photon excitation spectrum was also obtained for the red fluorescent protein mCherry (1 μM), in the same HEPES buffer. All excitation spectra are corrected for the wavelength-dependent transmission of the dichroic and band-pass filters, and quantum efficiency of the detector.

General cell culture and fluorescence microscopy. COS7 and U2OS cells (ATCC) were cultured in Dulbecco's modified Eagle medium (DMEM, phenol red-free; Life Technologies) supplemented with 10% (vol/vol) FBS (Life Technologies), 1 mM GlutaMAX (Life Technologies) and maintained at 37 °C in a humidified 5% (vol/vol) CO₂ environment. The COS7 cells have integrated a histone H2B-HaloTag expressing plasmid via the piggyback transposase (that is, H2B-Halo cells), and the U2OS cells have integrated a Sec61 β -HaloTag expressing plasmid via the piggyback transposase. Both cells were kept under the selection of 500 $\mu\text{g/ml}$ Geneticin (Life Technologies). Cell lines undergoes regular mycoplasma testing by the Janelia Cell Culture Facility. Cells were imaged on confocal microscopes in the Janelia Imaging Facility (Zeiss LSM 710, W Plan APO 20 \times /1.8 D -or- Zeiss LSM 880, C-APO 40 \times /1.2 W Corr FCS M27) using the indicated filter sets.

Comparison of JF₅₄₉ and JF₅₂₅. For the dye loading comparison (Fig. 1j), H2B-Halo COS7 cells were stained for varying amounts of time with 100 nM of either JF₅₂₅-HaloTag ligand **13** or JF₅₄₉-HaloTag ligand **14**. The dye was washed from the cells and subsequently labeled with JF₆₄₆-HaloTag ligand **26** at 1 μ M for 30 min. Fluorescence of JF₆₄₆-HaloTag ligand was quantified from the nuclear signals in summed confocal image stacks collected with 633 nm Ex/638–759 nm Em and analyzed using Fiji⁵⁰. The integrated density of the nuclear signal was corrected by subtracting the integrated density of adjacent background regions. Labeling is expressed as the percent of the JF₆₄₆-HaloTag fluorescence displaced by the JF₅₂₅- and JF₅₄₉-HaloTag ligands. The nuclear staining of these cells by the JF₅₂₅-HaloTag ligand (Fig. 1i) is displayed as a maximum intensity projection of confocal image stacks, 514 nm Ex/530–657 Em.

Comparison of JF₅₀₃ and other 488-nm-excited dyes. H2B-Halo COS7 cells were labeled with 200 nM of JF₅₀₃-HaloTag ligand **17**, HaloTag R110Direct ligand (**18**, Promega), or HaloTag ligand **19** (ref. 28), over a time course of 0–2 h. Cells were washed 2 \times with phosphate-buffered saline (PBS) and fixed with 4% (wt/vol) paraformaldehyde in 0.1 M phosphate for 30 min, followed by two more washes with PBS. Cells were imaged using confocal microscopy with 488 nm Ex/515–565 nm Em. The nuclear staining of these cells by the JF₅₀₃-HaloTag ligand (**17**; Fig. 2c) is displayed as a maximum intensity projection of confocal image stacks. Corrected nuclear fluorescence was calculated as above to determine the cell loading profile (Supplementary Fig. 2e). To test the relative bleaching rates of these three dyes under imaging conditions (Fig. 2d), cells were stained and fixed as previously described for 2 h and then bleached with 488 nm at twice the typical excitation power and imaged after each of 70 cycles. Bleached fluorescence data are normalized to the initial fluorescence levels.

Comparison of HaloTag ligands 22, 23 and 26–28 in cells. H2B-Halo COS7 cells were labeled with 250 nM of JF₆₀₈-HaloTag ligand (**22**), JF₅₈₅-HaloTag ligand (**23**), JF₆₄₆-HaloTag ligand (**26**), JF₆₃₅-HaloTag ligand (**27**) or SiTMR-HaloTag ligand (**28**; Supplementary Fig. 2k) and imaged by confocal microscopy using 594 nm Ex/599–734 nm Em (JF₆₀₈ and JF₅₈₅) or 633 nm Ex/638–759 nm Em (JF₆₄₆, JF₆₃₅, or SiTMR). All five samples were imaged via confocal microscopy without washing out the dyes. Signal to background (S/B) ratios were determined using the mean fluorescence of the nuclei relative to a region adjacent to each nuclei using Fiji⁵⁰ ($n = 152$ –275 areas as noted; Fig. 2h,i,m,n and Supplementary Fig. 2l).

Staining with SNAP-tag ligands. COS7 cells were transfected with histone H2B-pSNAP-tag (New England Biolabs) and stable integration of this plasmid was selected for using 600 μ g/ml Geneticin (Life Technologies). This cell line expresses the histone H2B protein fused to the 26m version of the SNAP-tag protein. Cells were stained with four different dyes as follows; JF₅₀₃-SNAP-tag ligand (**20**, 2 μ M for 90 min), JF₅₂₅-SNAP-tag ligand (**15**, 3 μ M for 30 min), JF₅₈₅-SNAP-tag ligand (**24**, 2 μ M for 3 h with 0.2% (wt/vol) Pluronic F-127), JF₆₃₅-SNAP-tag ligand (**29**, 2 μ M for 2 h with 0.2% (wt/vol) Pluronic F-127). After staining, cells were washed three times with complete media, followed by a 20-min

incubation in a 37 °C, 5% CO₂, humidified incubator. The media was replaced again immediately before imaging.

Multiplexed imaging using HaloTag and SNAP-tag. U2OS cells expressing Sec61 β -HaloTag fusion were transfected with either histone H2B-SNAP-tag piggybac or TOMM20-pSNAPf plasmids using Lipofectamine 2000 (ThermoFisher). Sec61 β encodes an endoplasmic reticulum membrane protein translocator protein, and TOMM20 encodes an outer mitochondrial membrane protein as part of a protein translocase complex. Live cells were simultaneously stained with combinations of JF₅₀₃-SNAP-tag ligand (**20**, 1 μ M) and JF₅₈₅-HaloTag ligand (**23**, 100 nM; Supplementary Fig. 2j) or JF₅₂₅-SNAP-tag ligand (**15**, 1 μ M) and JF₆₃₅-HaloTag ligand (**27**, 100 nM, Supplementary Fig. 2o) for 60 min. Cells were fixed with 4% paraformaldehyde (20 min), and subsequently stained with JF₆₄₆-Hoechst³³ (5 μ M, 30 min), as indicated, before imaging.

Cell viability assays. The effects of various Janelia Fluor ligand compounds on cell viability were tested using the tetrazolium dye 3-(4,5-dimethylthiazol-2-yl)-2,5-diphenyltetrazolium bromide (MTT, Supplementary Fig. 2c). This colorimetric cell viability assay relies on NAD(P)H-dependent oxidoreductase enzymes that reduce the dye to an insoluble and highly absorbing formazan⁵¹. COS7 cells were plated at 1.5×10^4 cells per well of a 96-well plate 24 h before the assay. Dyes were applied to cells at different concentrations to span standard labeling conditions in live cells ($n = 3$). HaloTag ligands **13**, **14**, **17**, **23**, **26** and **27** were applied for 1 h and SNAP-tag ligands **15**, **20**, **24** and **29** were applied for 3 h before addition of MTT to reflect typical maximum staining times for these dyes.

Staining of *Drosophila* larvae. The CNS of third instar *Drosophila melanogaster* larvae were dissected in physiological saline. For the JF₆₃₅-HaloTag ligand staining (Fig. 3a,b and Supplementary Fig. 3a,c), we used larva expressing a previously described⁵² HaloTag containing a myristoylation sequence in the ‘Basin’ neurons under control of the enhancer fragment R72F11³⁴. The isolated nervous system was incubated in physiological saline containing 1 μ M JF₆₃₅-HaloTag ligand (**27**) for 10 min at ambient temperature (22 ± 2 °C). For the pan-neuronal comparison (Supplementary Fig. 3b), this animal expressed GCaMP6s via the Gal4/UAS system using a 57C10-Gal4 driver line. The specimens were then embedded in agarose and imaged with the SiMView light-sheet microscope³⁵. The VNC zoomed images for direct comparison (Supplementary Fig. 3a,b) show the raw image data after fusion and deconvolution, whereas the full image of JF₆₃₅-HaloTag ligand labeling (Fig. 3a,b, Supplementary Fig. 3c) additionally uses filtering and gamma correction to show neuronal morphologies more clearly.

General information for mouse *in vivo* experiments. Male mice, 3–8 months old, were used for viral infection, dye injection and *in vivo* imaging of neurons in the visual cortex (V1): the Scnn1a-Tg3-Cre (Jax no. 009613) line was used for imaging in layer 4 cortical neurons (L4); and Rbp4-Cre mice (MMRRC no. 031125-UCD) were used for imaging in layer 4 cortical neurons (L5) neurons. All experimental protocols were conducted according to the National Institutes of Health guidelines for animal research

and were approved by the Institutional Animal Care and Use Committee at the Janelia Research Campus, HHMI.

Cranial window implant and virus injection. A craniotomy was carried out at the same time as the virus injection to provide optical access for *in vivo* imaging experiments. Mice were anesthetized with isoflurane (1–2% (vol/vol) in O₂) and given the analgesic buprenorphine (SC, 0.3 mg/kg). Using aseptic technique, a 3.5 mm-diameter craniotomy was made over the left V1 region of the brain of anaesthetized mouse (center: 3.4 mm posterior to Bregma; 2.7 mm lateral from midline). The dura was left intact. HaloTag and GCaMP6s was cotransduced using the viral vector: AAV2/1.synapsin.FLEX.GCaMP6s.P2A.HaloTag.WPRE (~5 × 10¹² infectious units per ml, 30 nl per site). The virus was injected using a glass pipette beveled at 45° with a 15–20-μm opening and back-filled with mineral oil. A fitted plunger controlled by a hydraulic manipulator (Narashige, MO10) was inserted into the pipette and used to load and inject the solution into six sites of left V1 (3.4–4.4 mm posterior to Bregma; 2.2–2.8 mm lateral from midline; ~0.5 mm distance between each injection site, 0.5 mm below pia). A cranial window made of a single glass coverslip (Fisher Scientific no. 1.5) was embedded in the craniotomy and sealed in place with dental acrylic. A titanium head-post was attached to the skull with cyanoacrylate glue and dental acrylic.

Dye administration *in vivo*. JF₅₈₅-HaloTag ligand (**23**) was first administered to mice 3–4 weeks after the cranial window installation and viral injection. Dye solution was prepared by first dissolving 100 nmol (76 μg) of **23** in 20 μl DMSO. After vortexing, 20 μl of a Pluronic F-127 solution (20% (wt/wt) in DMSO) was added and this stock solution was diluted into 100 μl or 200 μl sterile saline for IV (tail vein) or IP injection, respectively.

***In vivo* wide-field imaging and analysis.** Mice were head-fixed and awake during the imaging period and were therefore habituated to experimental handling and head fixation starting 1-week post-surgery. During each habituation session, mice were head-fixed onto the sample stage with body restrained under a half-cylindrical cover. The habituation procedure was repeated 3–4 times for each animal for a duration of 15–60 min. For *in vivo* wide-field imaging, an external fluorescence light source (Leica EL6000, Leica) was used for excitation of GCaMP6s (green channel) and JF₅₈₅-HaloTag ligand (red channel). Images were acquired via Leica Application Suite 4.5 (Leica). Wide-field images in green (1-s exposure) and red (4-s exposure) channels were acquired at multiple time intervals over 2 weeks under the same imaging conditions and the images were aligned with the Stackreg plugin in ImageJ. The mean values in the same area of red and green channels were plotted to track the labeling kinetics and turnover of JF₅₈₅-HaloTag *in vivo*.

***In vivo* two-photon imaging and analysis.** For *in vivo* two-photon imaging, GCaMP6s and JF₅₈₅-HaloTag were excited at 940 nm and 1,100 nm, respectively, using a femtosecond laser source (InSight DeepSee, Spectra-Physics), and imaged using an Olympus 25×, 1.05 NA objective and a homebuilt two-photon microscope⁵³. Images were acquired from 200 to 550 μm below the pia with post-objective power ranging between 20 and 60 mW. No photobleaching or photodamage of tissue was observed.

Typical imaging settings were composed of 256 × 256 pixels, with 1.2 μm per pixel, and a ~3-Hz frame rate. The time-lapse calcium images of spontaneous neuronal activity in awake, head fixed mice were recorded and analyzed with custom programs written in MATLAB (Mathworks). Lateral motion present in head-fixed awake mice was corrected using a cross-correlation-based registration algorithm⁵⁴, where cross-correlation was calculated to determine frame shift in x and y directions. Cortical neurons were outlined by hand as regions of interest (ROIs). The fluorescence time course of each ROI was used to calculate its calcium transient as $\Delta F/F$ (%) = $(F - F_0)/F_0 \times 100$, with the baseline fluorescence F_0 being the mode of the fluorescence intensity histogram of this ROI. For the Pearson correlation coefficient calculation, the JF₅₈₅ (red channel) and GCaMP6s (green channel) fluorescence signals in each ROI were averages from 1,000 imaging frames (3 Hz).

Statistics. For spectroscopy measurements (Figs. 1e,f and 2g,i, Table 1, and Supplementary Fig. 1) reported *n* values for absorption spectra, extinction coefficient (ϵ) and quantum yield (Φ) represent measurements of different samples prepared from the same dye DMSO stock solution. For the cell loading experiment (Fig. 1j) the following reported *n* values represent the number of intensity values measured from three fields of view for the time points at 30 s, 1 min, 2 min, 3 min and 4 min, respectively: JF₅₂₅-HaloTag ligand **13**: *n* = 112, 120, 130, 114, 128; JF₅₄₉-HaloTag ligand **14**: *n* = 135, 129, 135, 158, 161. For the reference stain using JF₆₄₆-HaloTag ligand *n* = 248. For cellular toxicity (Supplementary Fig. 2c) assays, reported *n* values represent different cell culture samples in separate microplate wells. For the contrast measurements (Fig. 2h,i,m,n and Supplementary Fig. 2l) reported *n* values represent intensity values measured from three fields of view for each dye type. For the IV and IP experiments (Fig. 3d), reported *n* = 3 values represent different fields of view taken via wide-field imaging. The one-way ANOVA analysis of spontaneous neuronal activity before and after dye administration (Fig. 3g) gave $F(3, 236) = 0.1204$.

Data availability. The data that support the findings of this study are provided in the Source Data files and are available from the corresponding author upon request.

A Life Science Reporting Summary is available online.

- Critchfield, F.E., Gibson, J.A. Jr. & Hall, J.L. Dielectric constant for the dioxane-water system from 20 to 35°. *J. Am. Chem. Soc.* **75**, 1991–1992 (1953).
- Suzuki, K. *et al.* Reevaluation of absolute luminescence quantum yields of standard solutions using a spectrometer with an integrating sphere and a back-thinned CCD detector. *Phys. Chem. Chem. Phys.* **11**, 9850–9860 (2009).
- Frisch, M.J. *et al.* Gaussian 09, revision D.01. (Gaussian, Wallingford, Connecticut, USA, 2009).
- Dreuw, A., Weisman, J.L. & Head-Gordon, M. Long-range charge-transfer excited states in time-dependent density functional theory require non-local exchange. *J. Chem. Phys.* **119**, 2943–2946 (2003).
- Jacquemin, D. *et al.* Assessment of the efficiency of long-range corrected functionals for some properties of large compounds. *J. Chem. Phys.* **126**, 144105 (2007).
- Guthmuller, J. & Champagne, B. Resonance Raman scattering of rhodamine 6G as calculated by time-dependent density functional theory: vibronic and solvent effects. *J. Phys. Chem. A* **112**, 3215–3223 (2008).

47. Setiawan, D., Kazaryan, A., Martoprawiro, M.A. & Filatov, M. A first principles study of fluorescence quenching in rhodamine B dimers: how can quenching occur in dimeric species? *Phys. Chem. Chem. Phys.* **12**, 11238–11244 (2010).
48. Mütze, J. *et al.* Excitation spectra and brightness optimization of two-photon excited probes. *Biophys. J.* **102**, 934–944 (2012).
49. Akerboom, J. *et al.* Optimization of a GCaMP calcium indicator for neural activity imaging. *J. Neurosci.* **32**, 13819–13840 (2012).
50. Schindelin, J. *et al.* Fiji: an open-source platform for biological-image analysis. *Nat. Methods* **9**, 676–682 (2012).
51. Mosmann, T. Rapid colorimetric assay for cellular growth and survival: application to proliferation and cytotoxicity assays. *J. Immunol. Methods* **65**, 55–63 (1983).
52. Kohl, J. *et al.* Ultrafast tissue staining with chemical tags. *Proc. Natl. Acad. Sci. USA* **111**, E3805–E3814 (2014).
53. Ji, N., Milkie, D.E. & Betzig, E. Adaptive optics via pupil segmentation for high-resolution imaging in biological tissues. *Nat. Methods* **7**, 141–147 (2010).
54. Sun, W., Tan, Z., Mensh, B.D. & Ji, N. Thalamus provides layer 4 of primary visual cortex with orientation- and direction-tuned inputs. *Nat. Neurosci.* **19**, 308–315 (2016).

Life Sciences Reporting Summary

Nature Research wishes to improve the reproducibility of the work that we publish. This form is intended for publication with all accepted life science papers and provides structure for consistency and transparency in reporting. Every life science submission will use this form; some list items might not apply to an individual manuscript, but all fields must be completed for clarity.

For further information on the points included in this form, see [Reporting Life Sciences Research](#). For further information on Nature Research policies, including our [data availability policy](#), see [Authors & Referees](#) and the [Editorial Policy Checklist](#).

Experimental design

1. Sample size

Describe how sample size was determined.

All quantitative imaging experiments were performed on replicate samples or fields of view as reported in the Methods and figure legends.

2. Data exclusions

Describe any data exclusions.

None

3. Replication

Describe whether the experimental findings were reliably reproduced.

N/A

4. Randomization

Describe how samples/organisms/participants were allocated into experimental groups.

N/A

5. Blinding

Describe whether the investigators were blinded to group allocation during data collection and/or analysis.

N/A

Note: all studies involving animals and/or human research participants must disclose whether blinding and randomization were used.

6. Statistical parameters

For all figures and tables that use statistical methods, confirm that the following items are present in relevant figure legends (or in the Methods section if additional space is needed).

n/a Confirmed

- ☒ The exact sample size (n) for each experimental group/condition, given as a discrete number and unit of measurement (animals, litters, cultures, etc.)
- ☒ A description of how samples were collected, noting whether measurements were taken from distinct samples or whether the same sample was measured repeatedly
- ☒ A statement indicating how many times each experiment was replicated
- ☒ The statistical test(s) used and whether they are one- or two-sided (note: only common tests should be described solely by name; more complex techniques should be described in the Methods section)
- ☒ A description of any assumptions or corrections, such as an adjustment for multiple comparisons
- ☒ The test results (e.g. P values) given as exact values whenever possible and with confidence intervals noted
- ☒ A clear description of statistics including central tendency (e.g. median, mean) and variation (e.g. standard deviation, interquartile range)
- ☒ Clearly defined error bars

See the web collection on [statistics for biologists](#) for further resources and guidance.

► Software

Policy information about [availability of computer code](#)

7. Software

Describe the software used to analyze the data in this study.

We used published or commercial software to perform the image analysis as stated in the Methods.

For manuscripts utilizing custom algorithms or software that are central to the paper but not yet described in the published literature, software must be made available to editors and reviewers upon request. We strongly encourage code deposition in a community repository (e.g. GitHub). *Nature Methods* [guidance for providing algorithms and software for publication](#) provides further information on this topic.

► Materials and reagents

Policy information about [availability of materials](#)

8. Materials availability

Indicate whether there are restrictions on availability of unique materials or if these materials are only available for distribution by a for-profit company.

We will deposit all plasmids in AddGene. The Janelia Fluor dyes will be distributed freely to all nonprofit researchers until commercialization.

9. Antibodies

Describe the antibodies used and how they were validated for use in the system under study (i.e. assay and species).

N/A

10. Eukaryotic cell lines

a. State the source of each eukaryotic cell line used.

All Cell Lines were from ATCC as stated in the Methods.

b. Describe the method of cell line authentication used.

N/A

c. Report whether the cell lines were tested for mycoplasma contamination.

The Janelia Cell Culture Facility regularly tests for mycoplasma contamination. This is stated in the Methods.

d. If any of the cell lines used are listed in the database of commonly misidentified cell lines maintained by [ICLAC](#), provide a scientific rationale for their use.

N/A

► Animals and human research participants

Policy information about [studies involving animals](#); when reporting animal research, follow the [ARRIVE guidelines](#)

11. Description of research animals

Provide details on animals and/or animal-derived materials used in the study.

Male mice, 3–8 months old, were used for viral infection, dye injection, and in vivo imaging of neurons in the visual cortex (V1): The Scnn1a-Tg3-Cre (Jax no. 009613) line was used for imaging in layer 4 cortical neurons (L4); and Rbp4-Cre mice (MMRRC no. 031125-UCD) were used for imaging in layer 4 cortical neurons (L5) neurons. All experimental protocols were conducted according to the National Institutes of Health guidelines for animal research and were approved by the Institutional Animal Care and Use Committee at the Janelia Research Campus, HHMI.

Policy information about [studies involving human research participants](#)

12. Description of human research participants

Describe the covariate-relevant population characteristics of the human research participants.

N/A